ELSEVIER

Available online at www.sciencedirect.com

SCIENCE DIRECT®

International Journal of Solids and Structures 42 (2005) 6299–6318

INTERNATIONAL JOURNAL OF SOLIDS and STRUCTURES

www.elsevier.com/locate/ijsolstr

Geometric functions of stress intensity factor solutions for spot welds in lap-shear specimens

D.-A. Wang [a], P.-C. Lin [b], J. Pan [b,*]

[a] *Institute of Precision Engineering, National Chung Hsing University, Taichung 402, Taiwan*
[b] *Department of Mechanical Engineering, The University of Michigan, Ann Arbor, MI 48109-2125, USA*

Received 22 June 2004; received in revised form 26 May 2005
Available online 20 July 2005

Abstract

In this paper, the stress intensity factor solutions for spot welds in lap-shear specimens are investigated by finite element analyses. Three-dimensional finite element models are developed for lap-shear specimens to obtain accurate stress intensity factor solutions. In contrast to the existing investigations of the stress intensity factor solutions based on the finite element analyses, various ratios of the sheet thickness, the half specimen width, the overlap length, and the specimen length to the nugget radius are considered in this investigation. The computational results confirm the functional dependence on the nugget radius and sheet thickness of the stress intensity factor solutions of [Zhang, S., 1997. Stress intensities at spot welds. International Journal of Fracture 88, 167–185; Zhang, S., 1999. Approximate stress intensity factors and notch stresses for common spot-welded specimens. Welding Journal 78, 173s–179s]. The computational results provide some geometric functions in terms of the normalized specimen width, the normalized overlap length, and the normalized specimen length to the stress intensity factor solutions of [Zhang, S., 1997. Stress intensities at spot welds. International Journal of Fracture 88, 167–185; Zhang, S., 1999. Approximate stress intensity factors and notch stresses for common spot-welded specimens. Welding Journal 78, 173s–179s] for lap-shear specimens. The computational results also indicate that when the spacing between spot welds decreases, the mode I stress intensity factor solution at the critical locations increases and the mode mixture of the stress intensity factors changes consequently. Finally, based on the analytical and computational results, the dimensions of lap-shear specimens and the corresponding approximate stress intensity factor solutions are suggested.

Keywords: Spot weld; Lap-shear specimen; Mixed mode; Stress intensity factor; Geometric functions; Fracture; Fatigue

---

[*] Corresponding author. Tel.: +1 734 764 9404; fax: +1 734 647 3170.
E-mail address: jwo@umich.edu (J. Pan).

0020-7683/$ - see front matter © 2005 Elsevier Ltd. All rights reserved.
doi:10.1016/j.ijsolstr.2005.05.037

1. Introduction

Resistance spot welding is widely used to join sheet metals for automotive components. The fatigue lives of spot welds have been investigated by many researchers in various types of specimens, for example, see Zhang (1999). Since the spot weld provides a natural crack or notch along the weld nugget circumference, fracture mechanics has been adopted to investigate the fatigue lives of spot welds in various types of specimens based on the stress intensity factor solutions at the critical locations of spot welds (Pook, 1975, 1979; Radaj and Zhang, 1991a,b, 1992; Swellam et al., 1994; Zhang, 1997, 1999, 2001). The stress intensity factors usually vary point by point along the circumference of spot welds in various types of specimens. Pook (1975, 1979) gave the maximum stress intensity factor solutions for spot welds in lap-shear specimens, coach-peel specimens, circular plates and other bending dominant plate and beam specimens. Swellam et al. (1994) proposed a stress index K_i by modifying their stress intensity factor solutions to correlate their experimental results for various types of specimens. Zhang (1997, 1999, 2001) obtained the stress intensity factor solutions for spot welds in various types of specimens in order to correlate the experimental results of spot welds in these specimens under cyclic loading conditions.

In order to obtain accurate stress and strain distributions and/or stress intensity factor solutions for spot welds in lap-shear specimens, finite element analyses have been carried out by various investigators (Radaj et al., 1990; Satoh et al., 1991; Deng et al., 2000; Pan and Sheppard, 2002, 2003). Radaj et al. (1990) used a finite element model where plate and brick elements are used for sheets and spot welds, respectively, to obtain the stress intensity factor solutions along the nugget circumference for the main cracks in various specimens. Satoh et al. (1991) conducted three-dimensional elastic and elastic–plastic finite element analyses to investigate the stress and strain distributions in the symmetry plane near spot welds in lap-shear specimens to identify the fatigue crack initiation sites under high-cycle and low-cycle fatigue loading conditions. Deng et al. (2000) conducted elastic and elastic–plastic three-dimensional finite element analyses to investigate the stress fields in and near the nuggets in lap-shear and symmetrical coach peel specimens to understand the effects of the nugget size and the thickness on the interface and nugget pull out failure modes. Pan and Sheppard (2002) also used a three-dimensional elastic–plastic finite element analysis to correlate the fatigue lives of spot welds to the cyclic plastic strain ranges for the material elements near the main notch in lap-shear specimens and modified coach-peel specimens. Pan and Sheppard (2003) conducted a three-dimensional finite element analysis to investigate the critical local stress intensity factor solutions for kinked cracks with a nearly elliptical shape emanating from the main notch along the nugget circumference in lap-shear specimens and modified coach-peel specimens.

Fig. 1 schematically shows a lap-shear specimen used to investigate the strength and fatigue lives of spot welds under shear dominant loading conditions. The weld nugget is idealized as a circular cylinder as shown in the figure. The lap-shear specimen has the thickness t, the width $2W$, the nugget radius b, the overlap length V of the upper and lower sheets, and the length L as shown in Fig. 1. Note that two spacers of

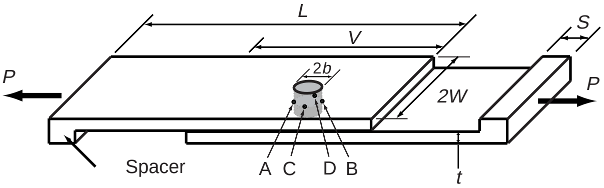

Fig. 1. A schematic plot of a lap-shear specimen. The applied force P is shown as the bold arrows. The weld nugget is idealized as a circular cylinder and shown as a shaded cylinder. The critical locations with the maximum mode I and II stress intensity factors are marked as point A and point B. The critical locations with the maximum mode III stress intensity factor are marked as point C and point D.

the length S are attached to the both ends of the lap-shear specimen to induce a pure shear to the interfacial plane of the nugget for the two sheets and to avoid the initial realignment during testing.

In this paper, we investigate the stress intensity factor solutions for spot welds in lap-shear specimens by a systematic finite element analysis. Three-dimensional finite element models based on the finite element model for two circular plates with connection (Wang et al., 2005) are used to obtain the stress intensity factor solutions for lap-shear specimens. The stress intensity factor solutions as functions of the ratios t/b, W/b and V/b are investigated. The stress intensity factor solutions of our computational results are compared with some existing computational and closed-form analytical stress intensity factor solutions for lap-shear specimens. Geometric functions in terms of the ratios W/b, L/b and V/b based on our computational results are suggested to the stress intensity factor solutions proposed by Zhang (1997, 1999).

2. Stress intensity factor solutions

Pook (1975) obtained stress intensity factor solutions at the critical locations (point A and point B as shown in Fig. 1) in lap-shear specimens of the thickness t and the nugget radius b under the applied force P as

$$K_{\mathrm{I}} = \frac{P}{b^{3/2}}\left[0.271(b/t)^{0.397}\right] \tag{1}$$

$$K_{\mathrm{II}} = \frac{P}{b^{3/2}}\left[0.282 + 0.265(b/t)^{0.710}\right] \tag{2}$$

Pook (1975) indicated that Eqs. (1) and (2) are applicable for $b/t \leqslant 5$ or $t/b \geqslant 0.2$.

As discussed in Swellam et al. (1994), the mode I stress intensity factor solution for spot welds was obtained from the solutions for two semi-infinite half spaces connected by a circular patch under an axial force and a moment in Tada et al. (2000). The mode II stress intensity factor solution for spot welds was approximated from the mode III stress intensity factor solution for two semi-infinite half spaces connected by a circular patch under a twisting moment in Tada et al. (2000). For lap-shear specimens, the stress intensity factor solutions at the critical locations (point A and point B as shown in Fig. 1) were proposed as (Swellam et al., 1994)

$$K_{\mathrm{I}} = \sqrt{\frac{2}{\pi}}\frac{1.061Pt}{b^{5/2}} \tag{3}$$

$$K_{\mathrm{II}} = \sqrt{\frac{2}{\pi}}\frac{0.354P}{b^{3/2}} \tag{4}$$

Zhang (1997, 1999) obtained the stress intensity factor K_{I} and K_{II} solutions at the critical locations (point A and point B as shown in Fig. 1) and the stress intensity factor K_{III} solution at the critical locations (point C and point D as shown in Fig. 1) for lap-shear specimens as

$$K_{\mathrm{I}} = \frac{\sqrt{3}P}{4\pi b\sqrt{t}} \tag{5}$$

$$K_{\mathrm{II}} = \frac{P}{\pi b\sqrt{t}} \tag{6}$$

$$K_{\mathrm{III}} = \frac{P}{\pi b\sqrt{2t}} \tag{7}$$

Note that these solutions were obtained from the closed-form stress solutions for a rigid inclusion under shear, center bending, counter bending and center twisting loading conditions in an infinite plate and the J integral formulation. The functional forms of Zhang's K_{I}, K_{II} and K_{III} solutions should be valid for lap-shear specimens of thin sheets with large ratios of W/b and V/b. Note that Zhang (1997, 1999) approximated the counter bending for the rigid inclusion by a center bending, namely, a moment applied to the rigid inclusion, to obtain the stress solutions for the derivation of the K_{I} solution.

In order to investigate the K_{I} solution for lap-shear specimens with finite geometry under counter bending, Lin et al. (to be submitted for publication) recently derived the K_{I} solution at the critical locations of a spot weld connecting at the center of two square plates under an applied counter bending moment M_0 along the two edges of each plate per unit length as

$$\begin{aligned} K_{\mathrm{I}} = {} & \frac{\sqrt{3}M_0}{XYt^{\frac{3}{2}}}\{2XY + X[-b^2(-1+v) + W^2(-1+v)] \\ & - Y[b^8(-1+v) + 2b^4W^4(1+v) - 4b^2W^6(1+v) + W^8(3+v)]\} \end{aligned} \tag{8}$$

where b is the radius of the spot weld, t is the thickness of the plate, $2W$ is the width of the plate, and v is the Poisson's ratio of the plate material. Here, X and Y are defined as

$$X = (-1+v)(b^4+W^4)^2 - 4b^2W^6(1+v) \tag{9}$$

$$Y = b^2(-1+v) - W^2(1+v) \tag{10}$$

In order to estimate the K_{I} solution for a "square" lap-shear specimen under the applied force P, the applied moment M_0 can be taken as $Pt/8W$. The details of the validation of the K_{I} solution in Eq. (8) are reported in Lin et al. (to be submitted for publication). Eq. (8) is used as the basis for the benchmark of the K_{I} solutions obtained from our computations.

3. Finite element analyses

In order to obtain accurate stress intensity factor solutions for spot welds in lap-shear specimens and to systematically examine the validity of the stress intensity factor solutions of Pook (1975), Swellam et al. (1994) and Zhang (1997, 1999), three-dimensional finite element analyses are carried out. Note that finite element analyses were carried out in Pook (1975), Cooper and Smith (1986), Radaj et al. (1990), Pan and Sheppard (2003) and Zhang (2004) for specific ratios of half specimen width to nugget radius, W/b, specific ratios of overlap length to nugget radius, V/b, and specific ratios of specimen thickness to nugget radius, t/b. No systematic investigation of the effects of t/b, W/b and V/b exists in the literature. The only systematic investigation of the effects of t/b by Pook (1975) appears to give significantly higher stress intensity factor solutions when compared to the other solutions (Zhang, 1997, 1999, 2004). Therefore, we emphasize our well-benchmarked finite element models used in this investigation. Our finite element models for lap-shear specimens are evolved from the three-dimensional finite element model for two circular plates with connection where a mesh sensitivity study was carried out to benchmark to a closed-form analytical stress intensity factor solution under axisymmetric loading conditions (Wang et al., 2005). The details to select an appropriate three-dimensional mesh for obtaining accurate stress intensity factor solutions for spot welds can be found in Wang et al. (2005).

Due to symmetry, only a half lap-shear specimen is considered. Fig. 2(a) shows a schematic plot of a half lap-shear specimen. The specimen has the thickness t (=0.65 mm), the length L (=77.3 mm), the half width W (=18.9 mm), and the nugget radius b (=3.2 mm) according to the dimensions of the lap-shear specimens used in Lin et al. (in press). The overlap length V of the upper and lower sheets is 47.1 mm. The two spacers have the length S (=4.6 mm). Both the upper and lower sheets have the same thickness. A Cartesian coordinate system is also shown in the figure. As shown in Fig. 2(a), a uniform displacement is applied in the $-x$ direction to the left edge surface of the specimen, and the displacements in the x, y and z directions for the

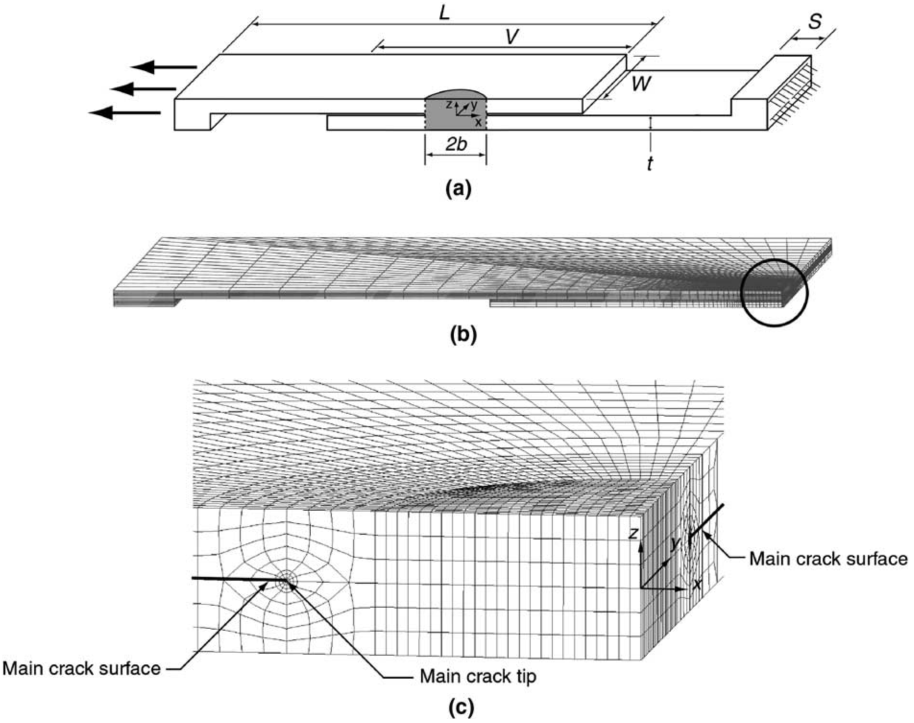

Fig. 2. (a) A schematic plot of a half lap-shear specimen with a uniform displacement applied to the left edge surface of the specimen shown as the bold arrows and the clamped boundary conditions for the right edge surface of the specimen. The shadow represents the half weld nugget. (b) A mesh for a left half finite element model. (c) A close-up view of the mesh near the main crack tip.

right edge surface of the specimen are constrained to represent the clamped boundary conditions in the experiment. The displacement in the y direction of the symmetry plane, the x–z plane, is constrained to represent the symmetry condition due to the loading conditions and the geometry of the specimen. Fig. 2(b) shows a mesh for a left half finite element model. Fig. 2(c) shows a close-up view of the mesh near the main crack tip. Note that the main crack is modeled as a sharp crack here. The three-dimensional finite element mesh near the weld nugget is evolved from the three-dimensional finite element mesh for two circular plates with connection as discussed in Wang et al. (2005). As shown in Fig. 2(c), the mesh near the center of the weld nugget is refined to ensure reasonable aspect ratios of the three-dimensional brick elements. The three-dimensional finite element model for the half lap-shear specimen has 34,248 20-node quadratic brick elements. The main crack surfaces are shown as bold lines in Fig. 2(c).

In this investigation, the weld nugget and the base metal are assumed to be linear elastic isotropic materials. The Young's modulus E is taken as 200 GPa, and the Poisson's ratio v is taken as 0.3. The commercial finite element program ABAQUS (Hibbitt et al., 2001) is employed to perform the computations. Brick elements with quarter point nodes and collapsed nodes along the crack front are used to model the $1/\sqrt{r}$ singularity near the crack tip.

First, the distributions of the stress intensity factor solutions along the circumference of the nugget are investigated here. Fig. 3 shows a top view of a nugget with a cylindrical coordinate system centered at the nugget center. An orientation angle θ is measured counterclockwise from the critical location of point B. Fig. 4 shows the normalized K_{I}, K_{II} and K_{III} solutions as functions of θ for the crack front along the nugget circumference based on our three-dimensional finite element computations for the lap-shear specimen with

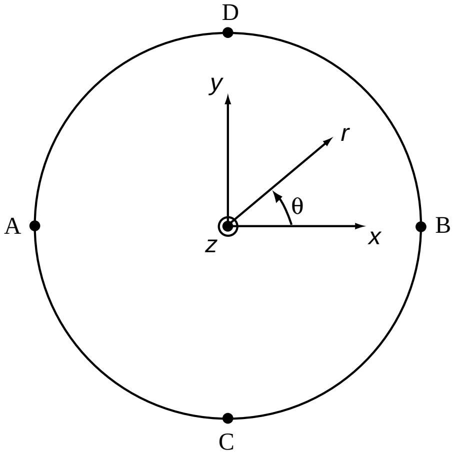

Fig. 3. A top view of a nugget with an orientation angle θ defined as shown. See Fig. 1 for the locations of points A–D.

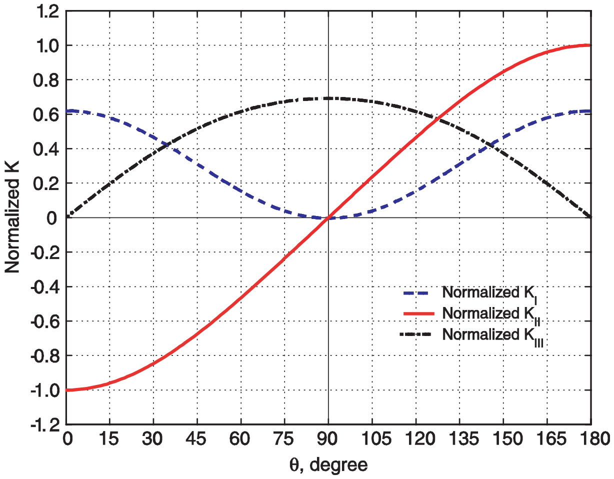

Fig. 4. The normalized K_I, K_{II} and K_{III} solutions as functions of θ for the crack front along the nugget circumference based on our three-dimensional finite element computations for the lap-shear specimen used in Lin et al. (in press).

$t/b = 0.2$, $W/b = 5.91$, $L/b = 24.16$ and $V/b = 14.72$. Note that the K_I, K_{II} and K_{III} solutions are normalized by the K_{II} solution at the critical location of point A ($\theta = 180°$). As shown in Fig. 4, the maxima of the K_I solution are located at point B ($\theta = 0°$) and point A ($\theta = 180°$), the maximum and minimum of the K_{II} solution are located at point A ($\theta = 180°$) and point B ($\theta = 0°$), respectively, and the maximum and minimum of the K_{III} solution are located at point D ($\theta = 90°$) and point C ($\theta = 270°$), respectively. The results shown in Fig. 4 indicate that K_{II} is the dominant stress intensity factor in lap-shear specimens under shear dominant loading conditions. The distributions of the stress intensity factor solutions along the circumference of the nugget as shown in Fig. 4 are similar to those in Radaj et al. (1990).

Next, we investigate the effects of the ratio of the sheet thickness t to the nugget radius b on the mode I and II stress intensity factor solutions at the critical locations (point A and point B as shown in Fig. 1) and the mode III stress intensity factor solution at the critical locations (point C and point D as shown in Fig. 1) for the specimens of Lin et al. (in press) with the ratio of $W/b = 5.91$ and $V/b = 14.72$. Note that the maximum magnitudes of the K_{I} and K_{II} occur at point A and point B, whereas the maximum magnitudes of the K_{III} occur at point C and point D. We develop different three-dimensional finite element models by changing the sheet thickness t with the nugget radius b being fixed. Fig. 5 shows the normalized K_{II} solutions at the critical locations (point A and point B as shown in Fig. 1) as functions of t/b based on our three-dimensional finite element computations and the analytical solutions of Pook (1975) in Eq. (2), Swellam et al. (1994) in Eq. (4), and Zhang (1997, 1999) in Eq. (6) under the applied load P. The K_{II} solutions are normalized by Zhang's solution in Eq. (6), denoted by $(K_{\mathrm{II}})_{\mathrm{Zhang}}$. Note that for this case, the K_{II} solution at point B is negative. But the magnitudes of the K_{II} solutions at points A and B are the same. The range of the ratio t/b is selected from 0.08 to 0.58 to represent the typical values for spot welds used in the automotive industry. As shown in Fig. 5, the normalized K_{II} solution based on our three-dimensional finite element computations appears to be relatively constant for the ratios of t/b considered. The normalized K_{II} solutions of Pook (1975) and Swellam et al. (1994) show significant deviations from the solutions based on our three-dimensional finite element computations and the analytical solution of Zhang (1997, 1999). Note that Pook's solution is applicable for $t/b \geqslant 0.2$ (Pook, 1975).

The results of our three-dimensional finite element computations confirm the functional dependence of Zhang's analytical K_{II} solution on the sheet thickness t and the nugget radius b. Zhang's analytical K_{II} solution will be later used as the basis to express the K_{II} solution for lap-shear specimens. Note that the K_{II} solution of Zhang (1997, 1999) is obtained from the closed-form stress solution for a rigid inclusion under shear and center bending loading conditions in an infinite plate and the J integral formulation. For a lap-shear specimen with a finite width $2W$, a finite specimen length L and a finite overlap length V, a deviation from the closed-form analytical solution is possible for finite values of W/b, L/b and V/b. Therefore, the K_{II} solution for lap-shear specimens should be written as

$$(K_{\mathrm{II}})_{\text{lap-shear}} = F_{\mathrm{II}}(W/b, L/b, V/b)\frac{P}{\pi b\sqrt{t}} \tag{11}$$

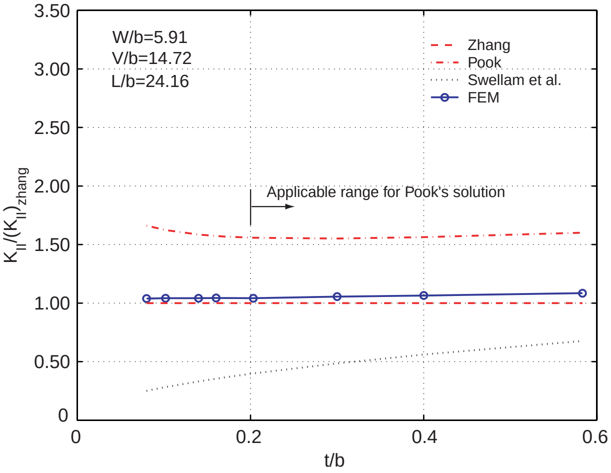

Fig. 5. The normalized K_{II} solutions at the critical locations (point A and point B as shown in Fig. 1) as functions of t/b based on our three-dimensional finite element computations and the analytical solutions for lap-shear specimens. The normalized K_{II} solutions based on our finite element computations and the analytical solutions in Eqs. (2), (4) and (6) are marked as FEM, Pook, Swellam et al., and Zhang, respectively.

where F_{II} is a geometric factor which is a function of W/b, L/b and V/b. Note that the value of L/b is usually very large for lap-shear specimens. For example, L/b is 24.16 for the specimens of Lin et al. (in press). The effects of large L/b 's on the K_{II} and K_{III} solutions should be small and therefore not considered initially. Also, V/b has a large value of 14.72 for the specimens of Lin et al. (in press). The effects of large V/b 's on the K_{II} and K_{III} solutions should be small and therefore are not considered initially. Here, for the geometry of the specimens of Lin et al. (in press) with $W/b = 5.91$, $L/b = 24.16$, $V/b = 14.72$ and $t/b = 0.20$, the geometric factor F_{II} is 1.04.

Fig. 6 shows the normalized K_{I} solutions at the critical locations (point A and point B as shown in Fig. 1) for the specimens of Lin et al. (in press) with $W/b = 5.91$, $L/b = 24.16$ and $V/b = 14.72$ as functions of t/b based on our three-dimensional finite element computations and the analytical solutions of Pook (1975) in Eq. (1), Swellam et al. (1994) in Eq. (3), and Zhang (1997, 1999) in Eq. (5) for lap-shear specimens under the applied load P. The K_{I} solutions are normalized by Zhang's K_{I} solution in Eq. (5), denoted by $(K_{\mathrm{I}})_{\mathrm{Zhang}}$. As shown in Fig. 6, the normalized K_{I} solution based on our three-dimensional finite element computations appears to be relatively constant for the range of the ratio t/b considered. The K_{I} solution based on our three-dimensional finite element computations is nearly 50% higher than that predicted by Zhang's K_{I} solution. The K_{I} solutions of Pook (1975) and Swellam et al. (1994) show significant deviations from our three-dimensional finite element computational solutions and Zhang's analytical K_{I} solution. Note again that the K_{I} solution of Zhang (1997, 1999) is based on the closed-form stress solution for a rigid inclusion under center bending in an infinite plate and the J integral formulation. The K_{I} solution based on our three-dimensional finite element computations confirms the dependence of Zhang's analytical K_{I} solution on the sheet thickness t and the nugget radius b. Therefore, Zhang's analytical K_{I} solution will be used as the basis to express the K_{I} solution for lap-shear specimens. For a lap-shear specimen with a finite width $2W$, a finite specimen length L and a finite overlap length V, the deviation of the computational solutions from the closed-form analytical solution is possible. Therefore, the K_{I} solution for lap-shear specimens can be written as

$$(K_{\mathrm{I}})_{\text{lap-shear}} = F_{\mathrm{I}}(W/b, L/b, V/b)\frac{\sqrt{3}P}{4\pi b\sqrt{t}} \tag{12}$$

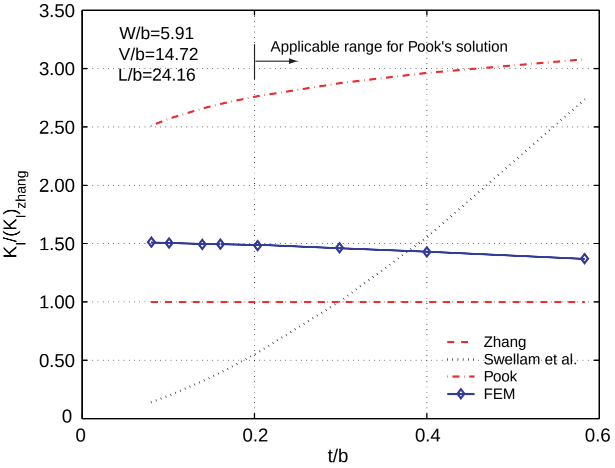

Fig. 6. The normalized K_{I} solutions at the critical locations (point A and point B as shown in Fig. 1) as functions of t/b based on our three-dimensional finite element computations and the analytical solutions for lap-shear specimens. The normalized K_{I} solutions based on our finite element computations and the analytical solutions in Eqs. (1), (3), (5) are marked as FEM, Pook, Swellam et al., and Zhang, respectively.

where F_{I} is a geometric factor which is a function of W/b, L/b and V/b. For the geometry of the specimens of Lin et al. (in press) with $W/b = 5.91$, $L/b = 24.16$, $V/b = 14.72$ and $t/b = 0.20$ considered in this investigation, the geometric factor is 1.49. Note that the K_{I} solutions of our computational results are substantially higher than those predicted by Zhang's analytical K_{I} solution. Therefore, the geometric factor F_{I} is needed.

Fig. 7 shows the normalized K_{III} solutions at the critical locations (point C and point D as shown in Fig. 1) for the specimens of Lin et al. (in press) with $W/b = 5.91$, $L/b = 24.16$ and $V/b = 14.72$ as functions of t/b based on our three-dimensional finite element computations and the analytical solution of Zhang (1997, 1999) in Eq. (7) for lap-shear specimens under the applied load P. The K_{III} solutions are normalized by Zhang's K_{III} solution in Eq. (7), denoted by $(K_{\mathrm{III}})_{\mathrm{Zhang}}$. As shown in Fig. 7, the normalized K_{III} solutions based on our three-dimensional finite element computations appear to be relatively constant for the range of the ratio t/b considered. The results of our three-dimensional finite element computations confirm the functional dependence of Zhang's analytical K_{III} solution on the sheet thickness t and the nugget radius b. Zhang's analytical K_{III} solution will be used as the basis to express the K_{III} solution for lap-shear specimens. Note that the K_{III} solution of Zhang (1997, 1999) is obtained from the closed-form stress solution for a rigid inclusion under twisting conditions in an infinite plate and the J integral formulation. For a lap-shear specimen with a finite width $2W$, a finite specimen length L and a finite overlap length V, a deviation from the closed-form analytical solution is possible for finite values of W/b, L/b and V/b. Therefore, the K_{III} solution for lap-shear specimens should be written as

$$(K_{\mathrm{III}})_{\text{lap-shear}} = F_{\mathrm{III}}(W/b, L/b, V/b)\frac{P}{\pi b\sqrt{2t}} \tag{13}$$

where F_{III} is a geometric factor which is a function of W/b, L/b and V/b. For the geometry of the specimens of Lin et al. (in press) with $W/b = 5.91$, $L/b = 24.16$, $V/b = 14.72$ and $t/b = 0.20$ considered in this investigation, the geometric factor F_{III} is 1.02.

As shown in Figs. 5–7, the K_{I}, K_{II} and K_{III} solutions from our computations show a slight dependence on t/b. This suggests that as t/b increases, the effects of the thickness increase, and the computational solutions will deviate from those based on the thin plate theory. In order to validate the closed-form K_{I}, K_{II} and K_{III}

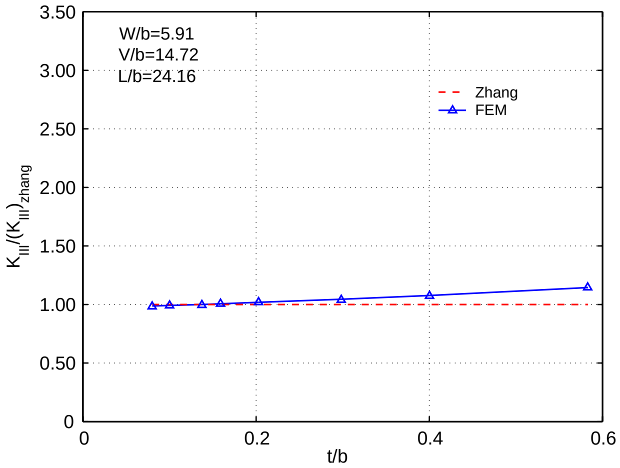

Fig. 7. The normalized K_{III} solutions at the critical locations (point C and point D as shown in Fig. 1) as functions of t/b based on our three-dimensional finite element computations and the analytical solution for lap-shear specimens. The normalized K_{III} solutions based on our finite element computations and the analytical solution of Zhang in Eq. (7) are marked as FEM and Zhang, respectively.

solutions based on the thin plate theory, we should pay more attention on the computational solutions for small t/b's. We continue the investigation based on the assumption that the geometry factors F_{I}, F_{II} and F_{III} have a weak dependence on t/b for small values of t/b.

As indicated in Eqs. (11)–(13), F_{I}, F_{II} and F_{III} should be functions of the three normalized length parameters W/b, L/b and V/b. The number of computations is too large for a full-scale numerical investigation of the three geometric functions F_{I}, F_{II} and F_{III} with the complex coupling effects of the three parameters W/b, L/b and V/b. Therefore, we choose a large value of L/b where the effects of the applied load clamping boundary is supposedly minimized. We also choose a large value of V/b where the free surface boundary condition is supposedly minimized. We take $L/b = 24.16$, $V/b = 14.72$ based on the specimens of Lin et al. (in press). As indicated in Lin et al. (to be submitted for publication), K_{I} is scaled by an applied counter bending moment M_0 along the plate edge per unit length. Therefore, the effects of the normalized specimen width W/b on K_{I} will be most significant.

Now, the effects of W/b on the geometric factors F_{I}, F_{II} and F_{III} are investigated. Fig. 8 shows the normalized K_{I} and K_{II} solutions at the critical locations (point A and point B as shown in Fig. 1) and the normalized K_{III} solution at the critical locations (point C and point D as shown in Fig. 1) as functions of W/b based on our three-dimensional finite element computations for $L/b = 24.16$, $V/b = 14.72$ and $t/b = 0.20$. The computational K_{I}, K_{II} and K_{III} solutions, denoted by $(K_{\mathrm{I}})_{\mathrm{FEM}}$, $(K_{\mathrm{II}})_{\mathrm{FEM}}$ and $(K_{\mathrm{III}})_{\mathrm{FEM}}$, are normalized by the K_{I}, K_{II} and K_{III} solutions of Zhang (1997, 1999), denoted by $(K_{\mathrm{I}})_{\mathrm{Zhang}}$, $(K_{\mathrm{II}})_{\mathrm{Zhang}}$ and $(K_{\mathrm{III}})_{\mathrm{Zhang}}$, respectively. Therefore, the normalized K_{I}, K_{II} and K_{III} solutions here represent the geometric factors F_{I}, F_{II} and F_{III} for $V/b = 14.72$, $L/b = 24.16$ and $t/b = 0.20$ according to Eqs. (12), (11) and (13), respectively. Note that we select a small value of $t/b = 0.20$ to avoid the effects of the thickness. Six ratios of W/b, namely, 2.05, 4.70, 5.66, 10.75, 15.59 and 25.27, are considered. Here, the nugget radius b, the nugget thickness t, the specimen length L, and the overlap length V are fixed whereas the half specimen width W is varied in the finite element models. Note that for the specimens of Lin et al. (in press), $W/b = 5.91$.

As shown in Fig. 8, F_{II} decreases slightly as W/b increases, and levels off as W/b is greater than 10. As W/b increases, F_{I} decreases significantly and appears to decrease slowly when W/b is greater than 25. F_{III} increases slightly as W/b increases, and levels off as W/b is greater than 10. It is important to note that when W/b is greater than 10, F_{II} is 1 and F_{III} is nearly 1, which indicates the accuracy of Zhang's analytical K_{II} and

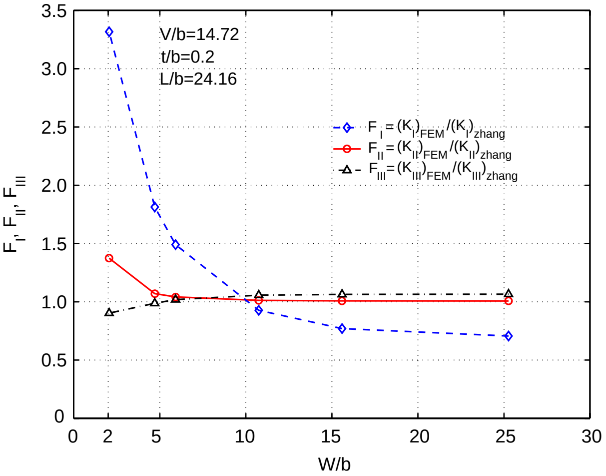

Fig. 8. The normalized K_{I} and K_{II} solutions at the critical locations (point A and point B as shown in Fig. 1) and the normalized K_{III} solution at the critical locations (point C and point D as shown in Fig. 1) as functions of W/b based on our three-dimensional finite element computations for $V/b = 14.72$, $t/b = 0.2$ and $L/b = 24.16$.

K_{III} solutions (Zhang, 1997, 1999). In contrast, when W/b increases to 25, F_{I} is nearly 0.71. As W/b further increases from 25, F_{I} seems to decrease slightly based on the trend of F_{I} as the function of W/b. F_{I} should continue to decrease as W/b increases based on the analytical solution in Eqs. (8)–(10). However, it seems that the rate of decrease slows down as W/b increases further from W/b equal to 15. As also shown in Fig. 8, when W/b decreases from 5, F_{I} and F_{II} increase significantly and F_{III} decreases slightly. For example, when W/b equals 2.05, the values of the geometric factors F_{I}, F_{II} and F_{III} are 3.32, 1.37 and 0.90, respectively.

Fig. 9 shows the normalized K_{I} and K_{III} solutions as functions of W/b based on our finite element computations. The K_{I} and K_{III} solutions are normalized by the corresponding K_{II} solutions for the corresponding W/b 's. As shown in Fig. 9, when W/b decreases from 5, the normalized K_{I} and K_{III} solutions change substantially. This suggests that when the spacing of spot welds decreases, the mixture of the modes at the critical locations changes significantly. Care should be taken for using the K_{I}, K_{II} and K_{III} solutions for closely spaced spot welds.

Note that Zhang (1997, 1999) used the analytical stress solution for a rigid inclusion under center bending in an infinite plate to approximate that under counter bending for the K_{I} solution in lap-shear specimens. The overestimation of the K_{I} solution for large ratios of W/b 's based on Zhang's analytical K_{I} solution can be attributed to this approximation. In order to estimate the K_{I} solution for lap-shear specimens, Lin et al. (to be submitted for publication) derived the K_{I} solution (Eq. (8)) at the critical locations for a spot weld at the center of two square plates under counter bending conditions. Fig. 10 shows the normalized K_{I} solutions as functions of W/b based on our finite element computations, denoted by $(K_{\mathrm{I}})_{\mathrm{FEM}}$ and the analytical solution of Lin et al. (to be submitted for publication) in Eq. (8), denoted by $(K_{\mathrm{I}})_{\mathrm{square}}$. The K_{I} solutions are normalized by Zhang's K_{I} solution, denoted by $(K_{\mathrm{I}})_{\mathrm{Zhang}}$. As shown in Fig. 10, the general trends of the K_{I} solutions based on our finite element computations and the analytical solution of Lin et al. (to be submitted for publication) are similar. For W/b ranging from 4.70 to 15.59, the K_{I} solutions of our finite element computations and Lin et al. (to be submitted for publication) are close to each other. As W/b increases from 15.59, the solutions of our finite element computations and Lin et al. (to be submitted for publication) start to deviate from each other. Note that the K_{I} solution of Lin et al. (to be submitted for publication) is obtained from the solution for a rigid inclusion in a square plate under counter bending, whereas our finite element models are for lap-shear specimens with different ratios of W/b and

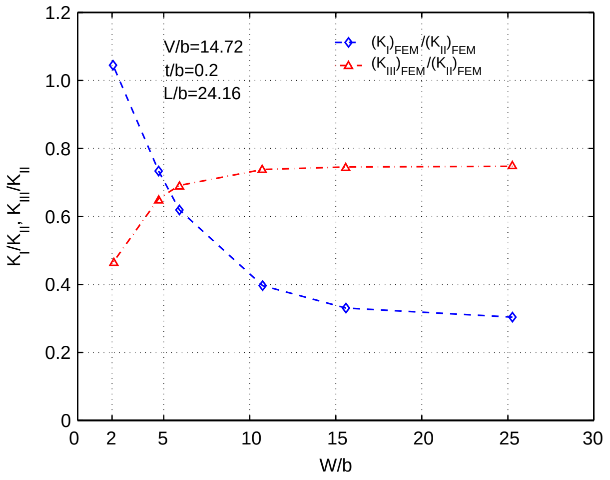

Fig. 9. The normalized K_{I} solution at the critical locations (point A and point B as shown in Fig. 1) and the normalized K_{III} solution at the critical locations (point C and point D as shown in Fig. 1) as functions of W/b based on our three-dimensional finite element computations for $V/b = 14.72$, $t/b = 0.2$ and $L/b = 24.16$.

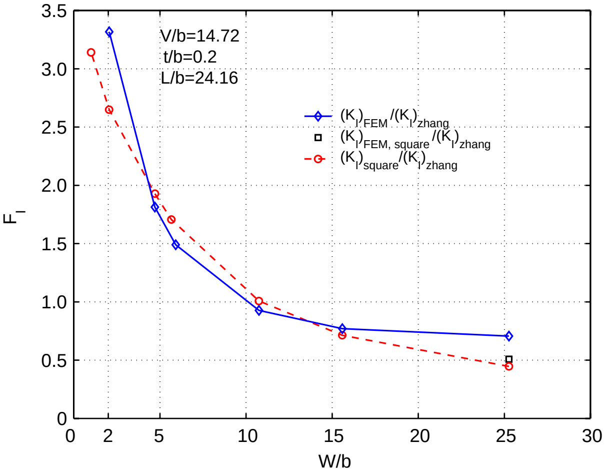

Fig. 10. The normalized K_I solutions at the critical locations (point A and point B as shown in Fig. 1) as functions of W/b based on our three-dimensional finite element computations and the analytical solution of Lin et al. (to be submitted for publication). The normalized K_I solutions based on our finite element computations and the analytical solution of Lin et al. (to be submitted for publication) are marked as $(K_I)_{FEM}$ and $(K_I)_{square}$, respectively. The normalized K_I solution based on our finite element computation for the case of $W/b = 25.27$, $V/b = 44.16$ and $L/b = 47.36$ is marked as $(K_I)_{FEM,square}$.

specific ratios of V/b (=14.72) and L/b (=24.16). In order to investigate the effects of V/L on the K_I solution, we performed a finite element computation for a nearly square shaped lap-shear specimen with $W = 80.85$ mm, $L = 151.54$ mm, $V = 141.30$ mm, $b = 3.20$ mm and $t = 0.65$ mm. For this case, $W/b = 25.27$, $V/b = 44.16$ and $L/b = 47.36$. The normalized K_I solution for this case is presented and marked by $(K_I)_{FEM,square}$ in Fig. 10. As shown in the figure, the result of this case is very close to the analytical solution of Lin et al. (to be submitted for publication) based on the solution for a rigid inclusion in a square plate with $W/b = 25.27$. Note that W represents the half width of the square plates.

Note that for large W/b's, the normalized K_I, K_{II} and K_{III} solutions do not change significantly as W/b changes as shown in Fig. 8. In order to understand the effects of the ratio of V/b on the K_I, K_{II} and K_{III} solutions, we develop finite element models for specimens with the ratio of $W/b = 25.27$, $L/b = 24.16$ and $t/b = 0.20$. Note that the number of computations is too high if we were to investigate the effects of V/b for different values of W/b. Therefore, we choose a large value of W/b with minimum width effects to avoid the complex coupling effects of W/b and V/b. We also choose a large value of L/b with minimum clamped boundary effects to avoid the complex coupling effects of L/b and V/b. These three-dimensional finite element models have different values of the overlap length V with the specimen length L, the nugget radius b, the nugget thickness t, and the half specimen width W being fixed.

Fig. 11 shows the normalized K_I and K_{II} solutions at the critical locations (point A and point B as shown in Fig. 1) and the normalized K_{III} solution at the critical locations (point C and point D as shown in Fig. 1) as functions of V/b based on our three-dimensional finite element computations. The computational K_I, K_{II} and K_{III} solutions, denoted by $(K_I)_{FEM}$, $(K_{II})_{FEM}$ and $(K_{III})_{FEM}$, are normalized by the K_I, K_{II} and K_{III} solutions of Zhang (1997, 1999), denoted by $(K_I)_{Zhang}$, $(K_{II})_{Zhang}$ and $(K_{III})_{Zhang}$, respectively. Therefore, the normalized K_I, K_{II} and K_{III} solutions here represent the geometric factors F_I, F_{II} and F_{III} for $W/b = 25.27$, $L/b = 24.16$ and $t/b = 0.20$ according to Eqs. (11)–(13), respectively. Six ratios of V/b, namely, 5.07, 9.42, 12.56, 14.72, 21.26 and 23.43, are considered. As shown in Fig. 11, F_I, F_{II} and F_{III} appear to be relatively constant when V/b is greater than 14.72. It should be noted that for the ratios of V/b ranging from 14.72 to 23.43, F_{II} is nearly 1, and F_{III} is nearly 1.05, which indicates the accuracy of

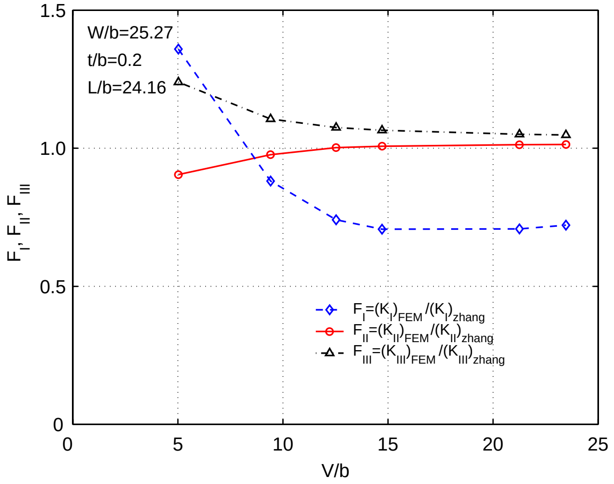

Fig. 11. The normalized K_{I} and K_{II} solutions at the critical locations (point A and point B as shown in Fig. 1) and the normalized K_{III} solution at the critical locations (point C and point D as shown in Fig. 1) as functions of V/b based on our three-dimensional finite element computations for $W/b = 25.27$, $t/b = 0.2$ and $L/b = 24.16$.

the analytical K_{II} and K_{III} solutions of Zhang (1997, 1999). In contrast, F_{I} is nearly 0.71 for the ratios of V/b ranging from 14.72 to 23.43. As also shown in Fig. 11, when V/b decreases further from 14.72, F_{I} increases significantly, F_{III} increases somewhat, and F_{II} decreases slightly.

Fig. 12 shows the normalized K_{I} and K_{III} solutions as functions of V/b based on our finite element computations. The K_{I} and K_{III} solutions are normalized by the corresponding K_{II} solutions for the corresponding V/b 's. As shown in Fig. 12, the normalized K_{I} and K_{III} solutions stay relatively constant when V/b is greater than 14.72. When V/b decreases from 14.72, the normalized K_{I} and K_{III} solutions increase substantially. When V/b decreases to 5.07, the K_{III} solution becomes comparable to the K_{II} solution, and the K_{I}

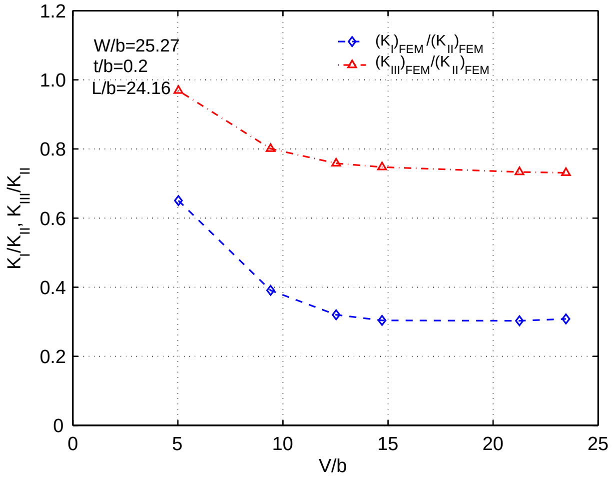

Fig. 12. The normalized K_{I} solution at the critical locations (point A and point B as shown in Fig. 1) and the normalized K_{III} solution at the critical locations (point C and point D as shown in Fig. 1) as functions of V/b based on our three-dimensional finite element computations for $W/b = 25.27$, $t/b = 0.2$ and $L/b = 24.16$.

solution is nearly 65% of the K_{II} solution. Therefore, the effects of the overlap length of lap-shear specimens can significantly affect the mixture of the modes at the critical locations for small V/b's.

We have examined the effects of W/b and V/b on the geometric factors F_{I}, F_{II} and F_{III}. Now we examine the effects of L/b on the geometric factors F_{I}, F_{II} and F_{III}. Finite element models for specimens with different L/b 's are developed for $W/b = 25.27$, $V/b = 14.72$ and $t/b = 0.20$. Here, we take large values of W/b and V/b with minimum width and overlap length effects to avoid the complex coupling effects of L/b, W/b and V/b. These three-dimensional finite element models have different values of the specimen length L with the nugget radius b, the nugget thickness t, the half specimen width W, and the overlap length V being fixed. Fig. 13 shows the normalized K_{I} and K_{II} solutions at the critical locations (point A and point B as shown in Fig. 1) and the normalized K_{III} solution at the critical locations (point C and point D as shown in Fig. 1) as functions of L/b based on our three-dimensional finite element computations. The computational K_{I}, K_{II} and K_{III} solutions, denoted by $(K_{\mathrm{I}})_{\mathrm{FEM}}$, $(K_{\mathrm{II}})_{\mathrm{FEM}}$ and $(K_{\mathrm{III}})_{\mathrm{FEM}}$, are normalized by the K_{I}, K_{II} and K_{III} solutions of Zhang (1997, 1999), denoted by $(K_{\mathrm{I}})_{\mathrm{Zhang}}$, $(K_{\mathrm{II}})_{\mathrm{Zhang}}$ and $(K_{\mathrm{III}})_{\mathrm{Zhang}}$, respectively. Therefore, the normalized K_{I}, K_{II} and K_{III} solutions here represent the geometric factors F_{I}, F_{II} and F_{III} for $W/b = 25.27$, $V/b = 14.72$ and $t/b = 0.20$ according to Eqs. (11)–(13), respectively. Five ratios of L/b, namely, 15, 20, 24.16, 30 and 80, are considered.

As shown in Fig. 13, F_{I}, F_{II} and F_{III} appear to be relatively constant when L/b is greater than 30 (or L/V is larger than 2.04). It should be noted that for the range of L/b considered, F_{II} is nearly 1, and F_{III} is nearly 1.06. The solutions agree with the analytical K_{II} and K_{III} solutions of Zhang (1997, 1999) for spot welds in plates of infinite size. However, as shown in Fig. 13, as L/b increases, F_{I} decreases and the decrease rate of F_{I} becomes smaller for L/b larger than 30. F_{I} approximately equals 0.63 for $L/b = 30$. This indicates that the effects of the length or the applied clamped boundary condition fade away for L/b larger than 30. For $L/b = 24.16$, the effects of the length is still there but not very large as shown in the figure. Therefore, the selection of $L/b = 24.16$, $V/b = 14.72$ based on the specimens of Lin et al. (in press) seems to be a good initial choice to avoid the effects of the clamped boundary and the free surface conditions.

Fig. 14 shows the normalized K_{I} and K_{III} solutions as functions of L/b based on our finite element computations. The K_{I} and K_{III} solutions are normalized by the corresponding K_{II} solutions for the corresponding L/b's. As shown in Fig. 14, the normalized K_{I} and K_{III} solutions stay relatively constant when L/b is

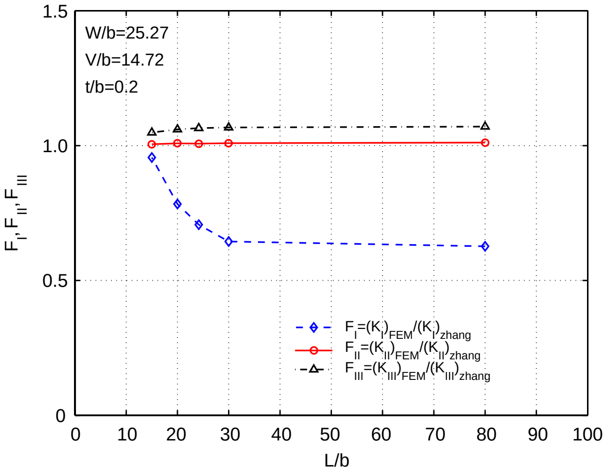

Fig. 13. The normalized K_{I} and K_{II} solutions at the critical locations (point A and point B as shown in Fig. 1) and the normalized K_{III} solution at the critical locations (point C and point D as shown in Fig. 1) as functions of L/b based on our three-dimensional finite element computations for $W/b = 25.27$, $V/b = 14.72$ and $t/b = 0.2$.

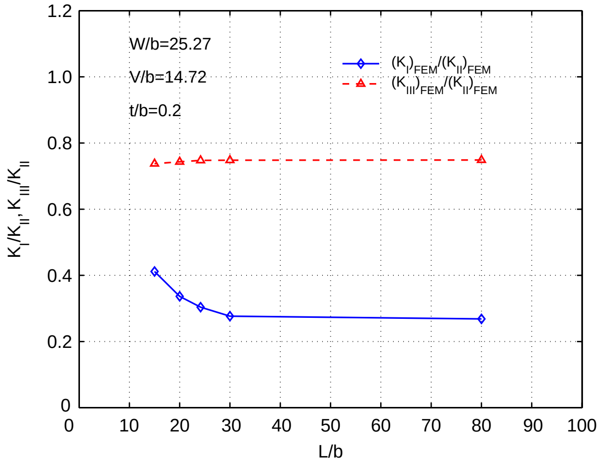

Fig. 14. The normalized K_I solution at the critical locations (point A and point B as shown in Fig. 1) and the normalized K_{III} solution at the critical locations (point C and point D as shown in Fig. 1) as functions of L/b based on our three-dimensional finite element computations for $W/b = 25.27$, $V/b = 14.72$ and $t/b = 0.2$.

greater than 30. When L/b decreases from $L/b = 30$, the normalized K_I solution increases substantially and the normalized K_{III} solution decreases slightly. When L/b decreases to 15, the K_{III} solution is nearly 74% of the K_{II} solution, and the K_I solution is nearly 41% of the K_{II} solution. Therefore, the effects of the specimen length of lap-shear specimens can significantly affect the mixture of the modes at the critical locations for small L/b's.

Based on the results of our finite element computations, the functional dependence of the geometric factors F_I, F_{II} and F_{III} on W/b, L/b and V/b are investigated under the conditions with minimum coupling effects of W/b, L/b and V/b. As shown in Fig. 8, the influence of W/b's on the geometric factors F_{II} and F_{III} is weak for $W/b > 15$. As shown in Fig. 11, the influence of V/b's on the geometric factors F_{II} and F_{III} is weak for $V/b > 15$. As shown in Fig. 13, the influence of L/b's on the geometric factors F_I, F_{II} and F_{III} is weak for $L/b > 30$. Therefore, for a lap-shear specimen with $W/b > 25$, $V/b > 15$ and $L/b > 30$, the dependence of the geometric factors F_I, F_{II} and F_{III} on W/b, V/b and L/b is minimum. This can be used as a design guideline for lap-shear specimens in the future.

In general, the values of V/b and L/b for specimens are large and therefore $V/b > 15$ and $L/b > 30$ are recommended for design of lap-shear specimens. Then the geometric functions presented in Fig. 8 for $L/b = 24.16$, $V/b = 14.72$ and $t/b = 0.20$ can be used to estimate the geometric function for specimens with different widths. Based on the results presented in Fig. 8 for engineering applications, we proposed that the lap-shear specimen should be made with $W/b > 5$, $V/b > 15$ and $L/b > 30$. The stress intensity factor solutions for specimens with the clamped loading conditions and the size requirements given above can be approximated in closed-form as

$$K_I = \frac{\sqrt{3}P}{8XYWt^{\frac{3}{2}}}\{2XY + X[-b^2(-1+v) + W^2(-1+v)] \\ - Y[b^8(-1+v) + 2b^4W^4(1+v) - 4b^2W^6(1+v) + W^8(3+v)]\} \tag{14}$$

$$K_{II} = \frac{P}{\pi b\sqrt{t}} \tag{15}$$

$$K_{III} = \frac{P}{\pi b\sqrt{2t}} \tag{16}$$

where X and Y are defined in Eqs. (9) and (10). Note that Eq. (14) is derived from the analytical solution in Eq. (8). Eq. (14) is a good approximate solution for the computational results shown in Fig. 10.

Now it is clear that the K_{I}, K_{II} and K_{III} solutions may be scaled by the nugget radius b and the sheet thickness t as in Eqs. 12,11,13 for large W/b's, L/b's and V/b's. For the specimen geometry with $W/b = 5.91$, $L/b = 24.16$ and $V/b = 14.72$ investigated here, the values of the geometric factors F_{I}, F_{II} and F_{III} are 1.49, 1.04 and 1.02, respectively. Recently, a two-dimensional elastic finite element analysis of a rigid inclusion with a radius of b in a finite width specimen with a width of $2W$ was performed by Lin et al. (2004). The results indicate that when the ratio of W/b is greater than 10, the radial stress at the critical locations of the nugget is close to the analytical solution for a rigid inclusion in an infinite plate. However, when the ratio of W/b decreases from 10, the radial stress at the critical locations of the nugget increases. The radial stress at the critical locations of the rigid inclusion is the starting point in the development of Zhang's stress intensity factor solutions (Zhang, 1997, 1999). It is clear that the analytical solutions of Zhang (1997, 1999) can characterize well the trends of the K_{I}, K_{II} and K_{III} solutions based on our three-dimensional finite element computations for large W/b's, L/b's and V/b's. However, the geometric factors F_{I}, F_{II} and F_{III} are needed to account for the effects of the specimen width $2W$, the specimen length L and the overlap length V of the upper and lower sheets.

Now we attempt to make a comparison of the existing computational stress intensity factor solutions with our computational results. We select the results from the three-dimensional finite element computation of Pan and Sheppard (2003) and a simplified finite element computation of Zhang (2004). First, we list the normalized K_{I}, K_{II} and K_{III} solutions at the critical locations by the analytical solutions of Zhang (1997, 1999) from our computations (listed as Wang et al., 2005), Pan and Sheppard (2003) and Zhang (2004) without consideration of the effects of t/b, W/b, L/b and V/b in Table 1. As listed in Table 1, we may not be able to judge the validity of the three solutions. Next, we consider the effects of W/b, L/b and V/b. Table 2 lists the values of t/b, W/b, L/b and V/b for the specimens used in our computation, Pan and Sheppard (2003) and Zhang (2004). Note that L/b is 33 for specimens used in Pan and Sheppard (2003) and L/b for specimens of Zhang (2004) is not available.

The geometry factors F_{I}, F_{II} and F_{III} for the solutions of Pan and Sheppard (2003) and Zhang (2004) are interpolated by a three-step approach. The interpolation method is approximate in nature since we do not have the results to account for the coupling effects of W/b, L/b and V/b in this investigation. First, the initial values of F_{I}, F_{II} and F_{III} are obtained from Fig. 8 by linear interpolation to account for the effects of W/b. Note that the results in Fig. 8 are for $L/b = 24.16$, $V/b = 14.72$ and $t/b = 0.2$. Then, the initial values of F_{I}, F_{II} and F_{III} are multiplied by the ratios of F_{I}, F_{II} and F_{III} for a given V/b to F_{I}, F_{II} and F_{III}

Table 1
Normalized computational K_{I}, K_{II} and K_{III} solutions at the critical locations by the analytical solutions of Zhang (1997, 1999) from our computations (listed as Wang et al., 2005), Pan and Sheppard (2003), and Zhang (2004)

	$K_{\mathrm{I}}/(K_{\mathrm{I}})_{\mathrm{Zhang}}$	$K_{\mathrm{II}}/(K_{\mathrm{II}})_{\mathrm{Zhang}}$	$K_{\mathrm{III}}/(K_{\mathrm{III}})_{\mathrm{Zhang}}$
Wang et al. (2005)	1.49	1.04	1.02
Pan and Sheppard (2003)	1.24	0.96	N/A
Zhang (2004)	1.19	1.02	1.01

Table 2
Values of F_{I}, F_{II} and F_{III} for different specimen geometries of Wang et al. (2005), Pan and Sheppard (2003), and Zhang (2004)

	t/b	W/b	V/b	L/b	F_{I}	F_{II}	F_{III}
Wang et al. (2005)	0.20	5.91	14.72	24.16	1.49	1.04	1.02
Pan and Sheppard (2003)	0.47	5.50	10.00	33	1.44	1.06	1.01
Zhang (2004)	0.40	8.00	12.80	NA	1.18	1.03	1.02

for $V/b = 14.72$ interpolated from the results presented in Fig. 11 for $W/b = 25.27$, $L/b = 24.16$ and $t/b = 0.2$. Finally, the values of F_{I}, F_{II} and F_{III} are multiplied by the ratios of F_{I}, F_{II} and F_{III} for a given L/b to F_{I}, F_{II} and F_{III} for $L/b = 24.16$ interpolated from the results presented in Fig. 13 for $W/b = 25.27$, $V/b = 14.72$ and $t/b = 0.2$. Since $L/b = 33$ for specimens used in Pan and Sheppard (2003), the ratios for F_{I}, F_{II} and F_{III} to account for the effects of L/b are nearly 1. Since the value of L/b for specimens used in Zhang (2004) is not available, the ratios to account for the effects of L/b for F_{I}, F_{II} and F_{III} are taken as 1. Table 2 lists the values of F_{I}, F_{II} and F_{III} for the three cases. As listed in the table, F_{I} is much greater than 1 for the three cases, whereas F_{II} and F_{III} are close to 1 for the three cases.

Table 3 lists the normalized K_{I}, K_{II} and K_{III} solutions by $F_{\mathrm{I}}(K_{\mathrm{I}})_{\mathrm{Zhang}}$, $F_{\mathrm{II}}(K_{\mathrm{II}})_{\mathrm{Zhang}}$ and $F_{\mathrm{III}}(K_{\mathrm{III}})_{\mathrm{Zhang}}$, respectively. As listed in Table 3, the normalized K_{I}, K_{II} and K_{III} solutions of Zhang (2004) are quite close to 1. This indicates that the geometric functions F_{I}, F_{II} and F_{III} based on our computational results are indeed needed and useful to scale the K_{I}, K_{II} and K_{III} solutions, and/or the solutions of Zhang (2004) are quite accurate. On the other hand, the normalized K_{I} and K_{II} solutions of Pan and Sheppard (2003) are not so close to 1. Note that the effects of t/b cannot be accounted for by F_{I}, F_{II} and F_{III}, and the coupling effects of W/b, L/b and V/b cannot be accounted for based on our interpolation method. The determination of F_{I}, F_{II} and F_{III} is based on the computational results for the small ratio of $t/b = 0.2$. The deviation from 1 of the normalized K_{I} and K_{II} solutions of Pan and Sheppard (2003) may be partly due to the large ratio of $t/b = 0.47$ compared to the ratio of $t/b = 0.2$ and 0.4 of Lin et al. (in press) and Zhang (2004), respectively.

Here, we attempt to account for the effects of t/b on the K_{I}, K_{II} and K_{III} solutions based on the weak functional dependence of K_{I}, K_{II} and K_{III} solutions on t/b shown in Figs. 5–7 for $W/b = 5.91$,

Table 3
Normalized computational K_{I}, K_{II} and K_{III} solutions at the critical locations by $F_{\mathrm{I}}(K_{\mathrm{I}})_{\mathrm{Zhang}}$, $F_{\mathrm{II}}(K_{\mathrm{II}})_{\mathrm{Zhang}}$ and $F_{\mathrm{III}}(K_{\mathrm{III}})_{\mathrm{Zhang}}$, respectively, for different specimen geometries of Wang et al. (2005), Pan and Sheppard (2003), and Zhang (2004)

	$K_{\mathrm{I}}/F_{\mathrm{I}}(K_{\mathrm{I}})_{\mathrm{Zhang}}$	$K_{\mathrm{II}}/F_{\mathrm{II}}(K_{\mathrm{II}})_{\mathrm{Zhang}}$	$K_{\mathrm{III}}/F_{\mathrm{III}}(K_{\mathrm{III}})_{\mathrm{Zhang}}$
Wang et al. (2005)	1.00	1.00	1.00
Pan and Sheppard (2003)	0.86	0.91	N/A
Zhang (2004)	1.01	0.99	0.99

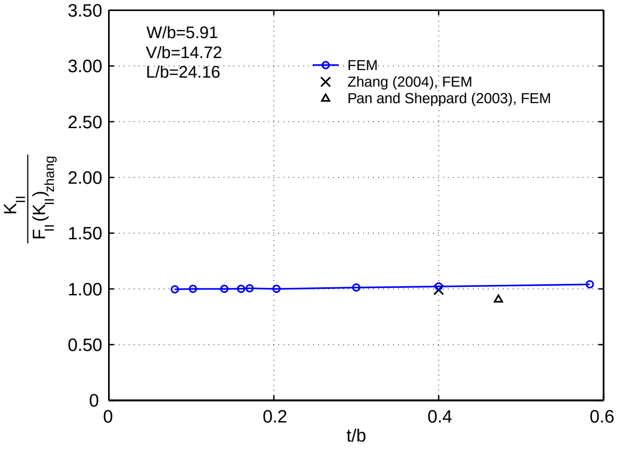

Fig. 15. The normalized K_{II} solutions at the critical locations (point A and point B as shown in Fig. 3) as a function of t/b based on our three-dimensional finite element computations, Pan and Sheppard (2003) and Zhang (2004). The normalized K_{II} solutions based on our finite element computations, Pan and Sheppard (2003) and Zhang (2004) are marked as FEM, Pan and Sheppard (2003), FEM, and Zhang (2004), FEM, respectively.

$L/b = 24.16$ and $V/b = 14.72$. Fig. 15 shows the normalized K_{II} solutions at the critical locations (point A and point B as shown in Fig. 1) based on our finite element computations, the three-dimensional finite element computations of Pan and Sheppard (2003), and the simplified finite element computation of Zhang (2004). Here, the K_{II} solutions are normalized by $F_{\mathrm{II}}(K_{\mathrm{II}})_{\mathrm{Zhang}}$. As shown in Fig. 15, the normalized K_{II} solution based on the simplified finite element computation of Zhang (2004) for $t/b = 0.4$, $W/b = 8$, and $V/b = 12.8$ is still nearly the same as that based on our finite element computations. The normalized K_{II} solution based on the three-dimensional finite element computation of Pan and Sheppard (2003) for $t/b = 0.47$, $W/b = 5.50$, $L/b = 33$ and $V/b = 10$ becomes lower than our computational K_{II} solution.

Fig. 16 shows the normalized K_{I} solutions at the critical locations (point A and point B as shown in Fig. 1) based on our computational results, the three-dimensional finite element computation of Pan and Sheppard (2003) and the simplified finite element computation of Zhang (2004). Here, the K_{I} solutions are normalized by $F_{\mathrm{I}}(K_{\mathrm{I}})_{\mathrm{Zhang}}$. As shown in Fig. 16, the normalized K_{I} solution based on the simplified finite element computation of Zhang (2004) for $t/b = 0.4$, $W/b = 8$, and $V/b = 12.8$ becomes slightly higher than our computational solution. The normalized K_{I} solution based on the three-dimensional finite element computation of Pan and Sheppard (2003) for $t/b = 0.47$, $W/b = 5.50$, $L/b = 33$ and $V/b = 10$ in fact becomes closer to our computational solution. Fig. 17 shows the normalized K_{III} solutions at the critical locations (point C and point D as shown in Fig. 1) based on our finite element computations and the simplified finite element computation of Zhang (2004). Here, the K_{III} solutions are normalized by $F_{\mathrm{III}}(K_{\mathrm{III}})_{\mathrm{Zhang}}$. As shown in Fig. 17, the normalized K_{III} solution based on the simplified finite element computation of Zhang (2004) for $t/b = 0.4$, $W/b = 8$, and $V/b = 12.8$ becomes slightly less than our computational solution.

Note that a mesh sensitivity study for the finite element model used in this investigation has been performed in Wang et al. (2005). The stress intensity factor solution based on the finite element model was well benchmarked to the analytical solution for circular plates and cylindrical cup specimens under axisymmetric loading conditions. On the other hand, Pan and Sheppard (2003) used the sub-modeling technique in ABAQUS (Hibbitt et al., 2001) to obtain their stress intensity factor solutions. Pan and Sheppard (2003) did not conduct a mesh sensitivity study to examine the accuracy of their stress intensity factor solutions with respect to any known analytical solutions. Therefore, more confidence can be placed on the accuracy of our stress intensity factor solutions. The differences of the stress intensity factor solutions of this

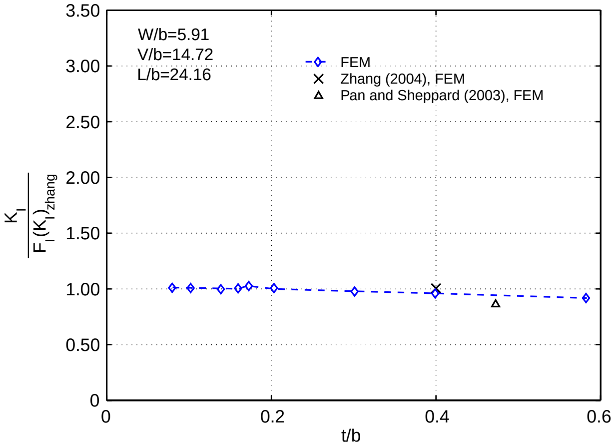

Fig. 16. The normalized K_{I} solutions at the critical locations (point A and point B as shown in Fig. 1) as a function of t/b based on our three-dimensional finite element computations, Pan and Sheppard (2003) and Zhang (2004). The normalized K_{I} solutions based on our finite element computations, Pan and Sheppard (2003) and Zhang (2004) are marked as FEM, Pan and Sheppard (2003), FEM, and Zhang (2004), FEM, respectively.

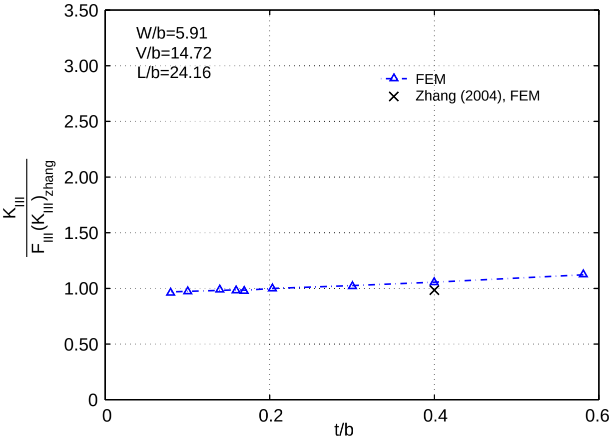

Fig. 17. The normalized K_{III} solutions at the critical locations (point C and point D as shown in Fig. 1) as a function of t/b based on our three-dimensional finite element computations and that of Zhang (2004). The normalized K_{III} solutions based on our finite element computations and Zhang (2004) are marked as FEM and Zhang (2004), FEM, respectively.

investigation and Pan and Sheppard (2003) shown in Figs. 15 and 16 may be due to the inaccuracy of the stress intensity factor solutions of the sub-modeling technique in Pan and Sheppard (2003) or the interpolation method from our limited sets of computational results.

4. Conclusions and discussions

Three-dimensional finite element analyses are carried out to investigate the stress intensity factor solutions for spot welds at the critical locations in lap-shear specimens. The mode I and II stress intensity factor solutions at the critical locations (point A and point B as shown in Fig. 1) and the mode III stress intensity factor solution at the critical locations (point C and point D as shown in Fig. 1) for spot welds in lap-shear specimens are obtained by three-dimensional finite element computations. The solutions can be correlated with those based on Zhang's solutions (Zhang, 1997, 1999) with new geometric functions in terms of the normalized specimen width, the normalized specimen overlap length and the normalized specimen length. The computational results confirm the functional dependence on the nugget radius and sheet thickness of the stress intensity factor solutions of Zhang (1997, 1999). The computational results indicate that as the normalized specimen width changes, the geometric functions change. The results suggest that when the spacing of spot welds decreases, the mode mixture of mode I, II and III stress intensity factors at the critical locations can change substantially. As the normalized overlap length or specimen length decreases, the geometric function for mode I stress intensity factor at the critical locations also changes significantly, and the mode mixture at the critical locations therefore changes significantly. Finally, based on the analytical and computational results, the dimensions of lap-shear specimens and the corresponding approximate stress intensity factor solutions are suggested. The geometric functions can be complex functions of the normalized sheet thickness, normalized specimen width, normalized specimen length and normalized specimen overlap length. Therefore, consideration of the geometric functions for stress intensity factor solutions can be useful to examine the existing fatigue data for spot welds in lap-shear specimens of various dimensions. The use of the stress intensity factor solutions to predict the fatigue lives of spot welds has been addressed in Newman and Dowling (1998), Lin and Pan (2004), Lin et al. (in press) and Lin et al. (2005) for fatigue life prediction of spot friction welds in lap-shear specimens.

Acknowledgment

Partial support of this work from a Ford/Army IMPACT project and a Ford University Research Program is greatly appreciated. Helpful discussions with S.-H. Lin of University of Michigan are greatly appreciated.

References

Cooper, J.F., Smith, R.A., 1986. Initial fatigue crack growth at spot-welds. In: International Conference on Fatigue of Engineering Materials and Structures, Sheffield, England, Mechanical Engineering Publication Ltd., London, England, vol. 2, 1986, pp. 283–288.

Deng, X., Chen, W., Shi, G., 2000. Three-dimensional finite element analysis of the mechanical behavior of spot welds. Finite Elements in Analysis and Design 35, 17–39.

Hibbitt, H.D., Karlsson, B.I., Sorensen, E.P., 2001. ABAQUS user manual, Version 6-2.

Lin, S.-H., Pan, J., 2004. Fatigue life prediction for spot welds in coach-peel and lap-shear specimens with consideration of kinked crack behavior. International Journal of Materials and Product Technology 20, 31–50.

Lin, S.-H., Pan, J., Wung, P., Chiang, J., in press. A fatigue crack growth model for spot welds in various types of specimens under cyclic loading conditions. International Journal of Fatigue.

Lin, P.-C., Lin, S.-H., Pan, J., 2004. Modeling of plastic deformation and failure near spot welds in lap-shear specimens. SAE Technical Paper 2004-01-0817, Society of Automotive Engineers, Warrendale, Pennsylvania.

Lin, P.-C., Wang, D.-A., Pan, J., to be submitted for publication. Mode I stress intensity factor solutions for spot welds in lap-shear specimens.

Lin, P.-C., Pan, J., Pan, T., 2005. Investigation of fatigue lives of spot friction welds in lap-shear specimens of aluminum 6111-T4 sheet based on fracture mechanics. SAE Technical Paper 2005-01-1250, Society of Automotive Engineers, Warrendale, Pennsylvania.

Newman, J.A., Dowling, N.E., 1998. A crack growth approach to life prediction of spot-welded lap joints. Fatigue & Fracture of Engineering Materials & Structures 21, 1123–1132.

Pan, N., Sheppard, S.D., 2002. Spot welds fatigue life prediction with cyclic strain range. International Journal of Fatigue 24, 519–528.

Pan, N., Sheppard, S.D., 2003. Stress intensity factors in spot welds. Engineering Fracture Mechanics 70, 671–684.

Pook, L.P., 1975. Fracture mechanics analysis of the fatigue behaviour of spot welds. International Journal of Fracture 11, 173–176.

Pook, L.P., 1979. Approximate stress intensity factors obtained from simple plate bending theory. Engineering Fracture Mechanics 12, 505–522.

Radaj, D., Zhang, S., 1991a. Stress intensity factors for spot welds between plates of unequal thickness. Engineering Fracture Mechanics 39, 391–413.

Radaj, D., Zhang, S., 1991b. Simplified formulae for stress intensity factors of spot welds. Engineering Fracture Mechanics 40, 233–236.

Radaj, D., Zhang, S., 1992. Stress intensity factors for spot welds between plates of dissimilar materials. Engineering Fracture Mechanics 42, 407–426.

Radaj, D., Zhaoyun, Z., Mohrmann, W., 1990. Local stress parameters at the weld spot of various specimens. Engineering Fracture Mechanics 37, 933–951.

Satoh, T., Abe, H., Nishikawa, K., Morita, M., 1991. On three-dimensional elastic–plastic stress analysis of spot-welded joint under tensile shear load. Transactions of the Japan Welding Society 22, 46–51.

Swellam, M.H., Banas, G., Lawrence, F.V., 1994. A fatigue design parameter for spot welds. Fatigue and Fracture of Engineering Materials & Structures 17, 1197–1204.

Tada, H., Paris, P.C., Irwin, G.R., 2000. The Stress Analysis of Cracks Handbook. ASME, New York.

Wang, D.-A., Lin, S.-H., Pan, J., 2005. Stress intensity factors for spot welds and associated kinked cracks in cup specimens. International Journal of Fatigue 27, 581–598.

Zhang, S., 1997. Stress intensities at spot welds. International Journal of Fracture 88, 167–185.

Zhang, S., 1999. Approximate stress intensity factors and notch stresses for common spot-welded specimens. Welding Journal 78, 173s–179s.

Zhang, S., 2001. Fracture mechanics solutions to spot welds. International Journal of Fracture 112, 247–274.

Zhang, S., 2004. A simplified spot weld model for finite element analysis. SAE Technical Paper 2004-01-0818, Society of Automotive Engineers, Warrendale, Pennsylvania.